

See discussions, stats, and author profiles for this publication at: <https://www.researchgate.net/publication/231272543>

Hydrate-Bearing Sediments from the Krishna–Godavari Basin: Physical Characterization, Pressure Core Testing, and Scaled Production Monitoring

ARTICLE *in* ENERGY & FUELS · NOVEMBER 2010

Impact Factor: 2.79 · DOI: 10.1021/ef100821t

CITATIONS

16

READS

34

3 AUTHORS:



Tae Sup Yun

Yonsei University

81 PUBLICATIONS 849 CITATIONS

SEE PROFILE



Dante Fratta

University of Wisconsin–Madison

84 PUBLICATIONS 311 CITATIONS

SEE PROFILE



J. Carlos Santamarina

King Abdullah University of Science and Tec...

240 PUBLICATIONS 3,901 CITATIONS

SEE PROFILE

Hydrate-Bearing Sediments from the Krishna–Godavari Basin: Physical Characterization, Pressure Core Testing, and Scaled Production Monitoring

Tae Sup Yun,^{*,†} Dante Fratta,[‡] and J. Carlos Santamarina[§]

[†]School of Civil and Environmental Engineering, Yonsei University, 262 Seongsan-ro, Seodaemun-gu, Seoul 120-749, Korea,
[‡]Geological Engineering Program, University of Wisconsin—Madison, 1415 Engineering Drive, Madison, Wisconsin 53706-1691,
United States, and [§]School of Civil and Environmental Engineering, Georgia Institute of Technology, 790 Atlantic Drive,
Northwest, Atlanta, Georgia 30332-0355, United States

Received June 29, 2010. Revised Manuscript Received October 14, 2010

Gas hydrate-bearing sediments recovered by pressure coring from the Krishna–Godavari Basin offshore India during the 2006 National Gas Hydrate Program (NGHP) expedition were characterized using the instrumented pressure testing chamber (IPTC). The IPTC studies provided longitudinal profiles of P- and S-wave velocities, electrical conductivity, and undrained penetration resistance. The formation consisted of fine-grained clayey sediments of high specific surface and high plasticity. X-ray images showed horizontal layering, pronounced heterogeneity from milli- to centimeter scales, with the presence of high-density nodules and both horizontal and sub-vertical gas hydrate lenses. Relative to reference values for sediments without hydrates, regions of high P- and S-wave velocities, low electrical conductivity, and high undrained shear strength were identified and correlated with regions of apparent high hydrate volume fractions in all tested specimens. Physical properties were monitored during the depressurization of pressure cores. The hydrate volume fraction was estimated to be 18.2%. The evolution of P-wave amplitude, electrical conductivity, and temperature showed gas generation and freshening upon phase transformation. The effect of sampling by pressure coring and the ensuing zero-effective stress condition were discussed.

Introduction

The Krishna–Godavari Basin covers the deltaic areas along the east coast of India, extends into the Bay of Bengal in the Indian Ocean, and forms a major graben and horst in the northeast–southwest direction.¹ It occupies an area of 20 000–28 000 km² onshore and 13 000–24 000 km² offshore. The basin was formed from the Late Carboniferous to the Quaternary, resulting in sediment layers up to several kilometers

thick.^{2–6} The sediment in this study area exhibits a high clay content of 50–70%, a high cation-exchange capacity, and a pH in the 7.3–8.5 range.^{7,8} Kaolinite, montmorillonite, and illite are the main clay minerals in these sediments.^{8,9} There are multiple oil- and gas-bearing structures in this petroliferous region, and the estimated hydrocarbon reserves exceed 2 billion tons.^{1,6} The gas is thermogenic from Permian coals and shales.^{2,10}

The first Indian National Gas Hydrate Program expedition (NGHP expedition 01) took place in the spring and summer of 2006 across the Indian Ocean shoreline along water depths ranging between 907 and 2674 m. It included 6 geophysical studies, drilling at 21 sites to depths of 718 m below the sea floor (mbsf), logging while drilling of 12 boreholes, and the recovery of both standard and pressure cores. Five pressure cores were recovered at site NGHP-01-21, located at 15°51.85'N, 81°50.08'E (water depth ~1049 m), transferred into storage chambers under hydrostatic pressure, and kept at 4 °C and 13 MPa fluid pressure for postcruise characterization and analysis. The date of pressure coring at NGHP-01-21 was August 12–15, 2006.

We tested three pressure cores at an onshore facility in Singapore between October 30 and November 7, 2006 (cores were maintained under ~13 MPa fluid pressure for 3 months). The test program included the measurement of elastic wave velocity, shear strength, and electrical conductivity, followed

*To whom correspondence should be addressed. Telephone: +82-2-2123-5805. Fax: 82-2-364-5300. E-mail: taesup@yonsei.ac.kr.

(1) Srivastava, A. K.; Singh, V.; Tiwary, D. N.; Rangachari, V. Impact of phase variations on quantitative AVO analysis: An example from Krishna Godavari Basin, India. *Leading Edge* **2006**, 25 (11), 1344–1358.

(2) Banerjee, V.; Mittal, A. K.; Agarwal, K.; Uniyal, A. K.; Chandra, K. Carbon isotope geochemistry of petroleum-associated gases in Krishna–Godavari Basin, India. *Org. Geochem.* **1994**, 21 (3–4), 373–382.

(3) Bastia, R.; Nayak, P. K. Tectonostratigraphy and depositional patterns in Krishna Offshore Basin, Bay of Bengal. *Leading Edge* **2006**, 25 (7), 839–845.

(4) Chatterjee, R.; Mukhopadhyay, M. Petrophysical and geomechanical properties of rocks from the oilfields of the Krishna–Godavari and Cauvery Basins, India. *Bull. Eng. Geol. Environ.* **2002**, 61 (2), 169–178.

(5) Gupta, S. K. Basin architecture and petroleum system of Krishna Godavari Basin, east coast of India. *Leading Edge* **2006**, 25 (7), 830–837.

(6) Rao, G. N. Sedimentation, stratigraphy, and petroleum potential of Krishna–Godavari Basin, east coast of India. *Am. Assoc. Pet. Geol. Bull.* **2001**, 85 (9), 1623–1643.

(7) Sarma, V. V.; Hyde, K. D.; Vittal, B. P. R. Frequency of occurrence of mangrove fungi from the east coast of India. *Hydrobiologia* **2001**, 455, 41–53.

(8) Swamy, M. L. Irrigation and drainage of problem soils in Krishna and Godavari Deltas of Andhra Pradesh. *Proceedings of the 12th International Congress on Irrigation and Drainage*; Fort Collins, CO, May 28–June 2, 1984.

(9) Basu, S. Clay mineralogy and pressure analysis from seismic information in Krishna–Godavari Basin, India. *Geophysics* **1990**, 55 (11), 1447–1454.

(10) Khan, M. S. R.; Sharma, A. K.; Sahota, S. K.; Mathur, M. Generation and hydrocarbon entrapment within Gondwanan sediments of the Mandapeta area, Krishna–Godavari Basin, India. *Org. Geochem.* **2000**, 31 (12), 1495–1507.

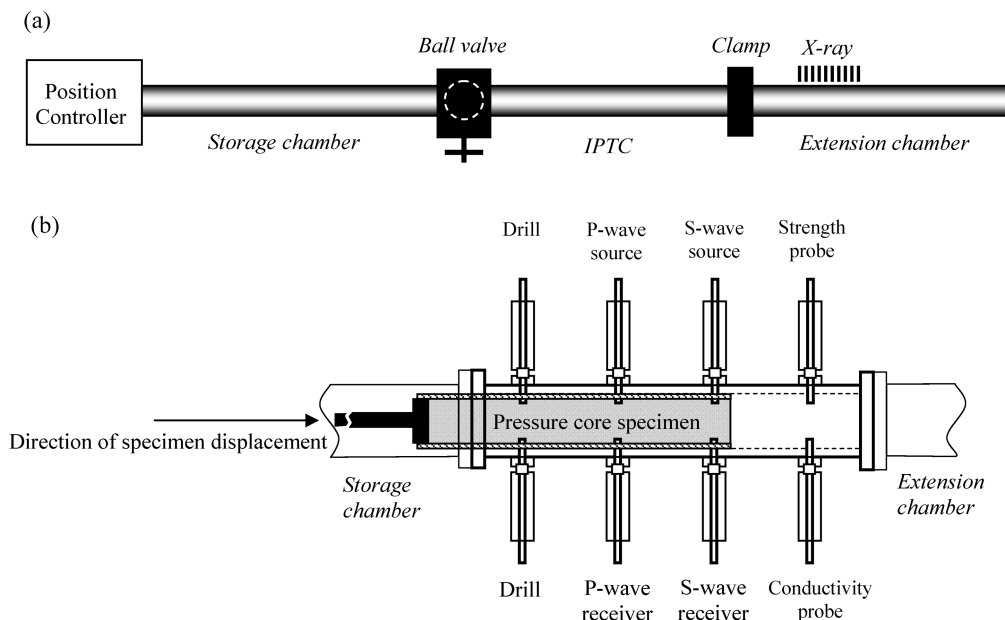


Figure 1. IPTC setup. (a) Complete manipulator and IPTC system deployed in the 6.1 m refrigerated container. (b) Measurement sequence. The holes in the plastic linear are drilled first, followed by the sequential introduction of instrumented P-wave, S-wave, push cone, and needle probe rods.

by fast depressurization of the sub-sampled core round. A brief description of devices used for this study follows.

Devices and Complementary Components

The pressure cores were never depressurized prior to the designated testing program, and the characterization of pressure cores was performed within the pressure–temperature stability field of hydrates. A specially designed “instrumented pressure testing chamber” (IPTC) was used to characterize the cores. The IPTC permits obtaining small-strain P-wave (using pinducers) and S-wave (using bender elements) velocities, large-strain undrained shear strength (using a cone-shaped penetrometer), electrical conductivity profile (using an electrical needle probe), and internal core temperature (using a thermocouple). The IPTC operation, instrumentation details, and earlier results gathered for pressure cores from the Gulf of Mexico are documented.^{11,12}

A 6.1 m long refrigerated container, deployed near the port in Singapore, housed the IPTC device and peripheral electronics, a single-side manipulator that facilitates the horizontal displacement and positioning of the pressure core inside the IPTC, and an X-ray imaging system. The manipulator and X-ray imaging system were built and operated by GeoTek, Inc. Figure 1a shows a schematic diagram of the IPTC setup and complementary devices. The storage chamber and supplementary devices were connected to the pressure controlled water pump to continuously maintain the designated *in situ* hydrostatic pressure of 13 MPa during the entire characterization stage.

The test sequence in the IPTC starts by transferring the pressure core from the storage chamber into the test string through a combination of ball valve manipulation and pressure equalization steps. Then, measurements were conducted at discrete intervals along the core. The interval was determined to capture the noticeable features in pressure cores (e.g., hydrate lens and nodules and sediment layers) based on the X-ray images prior

to the characterization. The test sequence at each location begins by drilling the core plastic linear, followed by P- and S-wave measurements across the core diameter, penetration of the cone-shaped strength probe to assess the sediment undrained strength, and insertion of the electrical needle probe to measure the sediment electrical conductivity (Figure 1b). The shear strength and electrical needle probes are driven ~25 mm into the sediment to minimize boundary effects.

Results

Index Properties: Depressurized Sediment. Gravimetric water content w_c , liquid limit w_L , plastic limit w_P , pH, specific surface S_a , sediment electrical conductivity σ_s , and complex dielectric permittivity κ^* were determined for the depressurized 21C-02E core sediments 1 month after the depressurization test was completed. Results are summarized in Table 1.

The values of specific surface range from $S_a = 87$ to $94 \text{ m}^2/\text{g}$. This specific surface corresponds to fine-grained clay minerals, such as illite and montmorillonite, in agreement with clay mineralogy data reported by Basu.⁹ The measured pH values range from 7.75 to 8, which presumably hint at the presence of carbonates.

The liquid limit w_L and plastic limit w_P reflect the soil mineralogy and fluid-dependent soil fabric effects and are used for the geomechanical classification of fine-grained sediments. The obtained values of the liquid limit $w_L = 73\text{--}75\%$, plastic limit $w_P = 34\text{--}36\%$, and plastic index $I_P = w_L - w_P = 40$ indicate that these sediments are classified as inorganic clays of high plasticity.

Physical Properties: Pressure Cores. Profiles of P- and S-wave velocities, electrical conductivity, and undrained shear strength are presented in Figures 2–4 for the three tested specimens. The corresponding X-ray images taken under pressure by GeoTek, Inc. are shown as well. Salient observations are summarized next.

Visual Observations. Lighter colors in X-ray images represent low-density materials, such as gas hydrate or cavities, while darker colors correspond to high-density sediments or

(11) Yun, T. S.; Narsilio, G. A.; Santamarina, J. C. Physical characterization of core samples recovered from Gulf of Mexico. *Mar. Pet. Geol.* **2006**, *23* (9–10), 893–900.

(12) Yun, T. S.; Narsilio, G. A.; Santamarina, J. C.; Ruppel, C. Instrumented pressure testing chamber for characterizing sediment cores recovered at *in situ* hydrostatic pressure. *Mar. Geol.* **2006**, *229* (3–4), 285–293.

Table 1. Index Properties of the 21C-02E Core Specimen

properties	values	device/technique
pH	7.75–8.5	nonbleeding pH strip (± 0.25)
specific surface (S_a , m^2/g)	87–94	methylene blue adsorption
liquid limit (w_L , %)	73–75	fall cone
plastic limit (w_P , %)	34–36	ASTM D4318-05
plastic index ($w_L - w_P$)	40	
gravimetric water content (w_c , %)	60–65	oven dry (ASTM D2216)
porosity (n)	0.61–0.63	computed from w_c assuming specific gravity $G_s = 2.65$
electrical conductivity (σ_e , S/m)	1.5–2	needle probe at ~ 10 kHz and high-frequency network analyzer at 1 GHz (HP 8752A)
dielectric permittivity (κ')	30–40	high-frequency network analyzer at 1 GHz (HP 8752A)

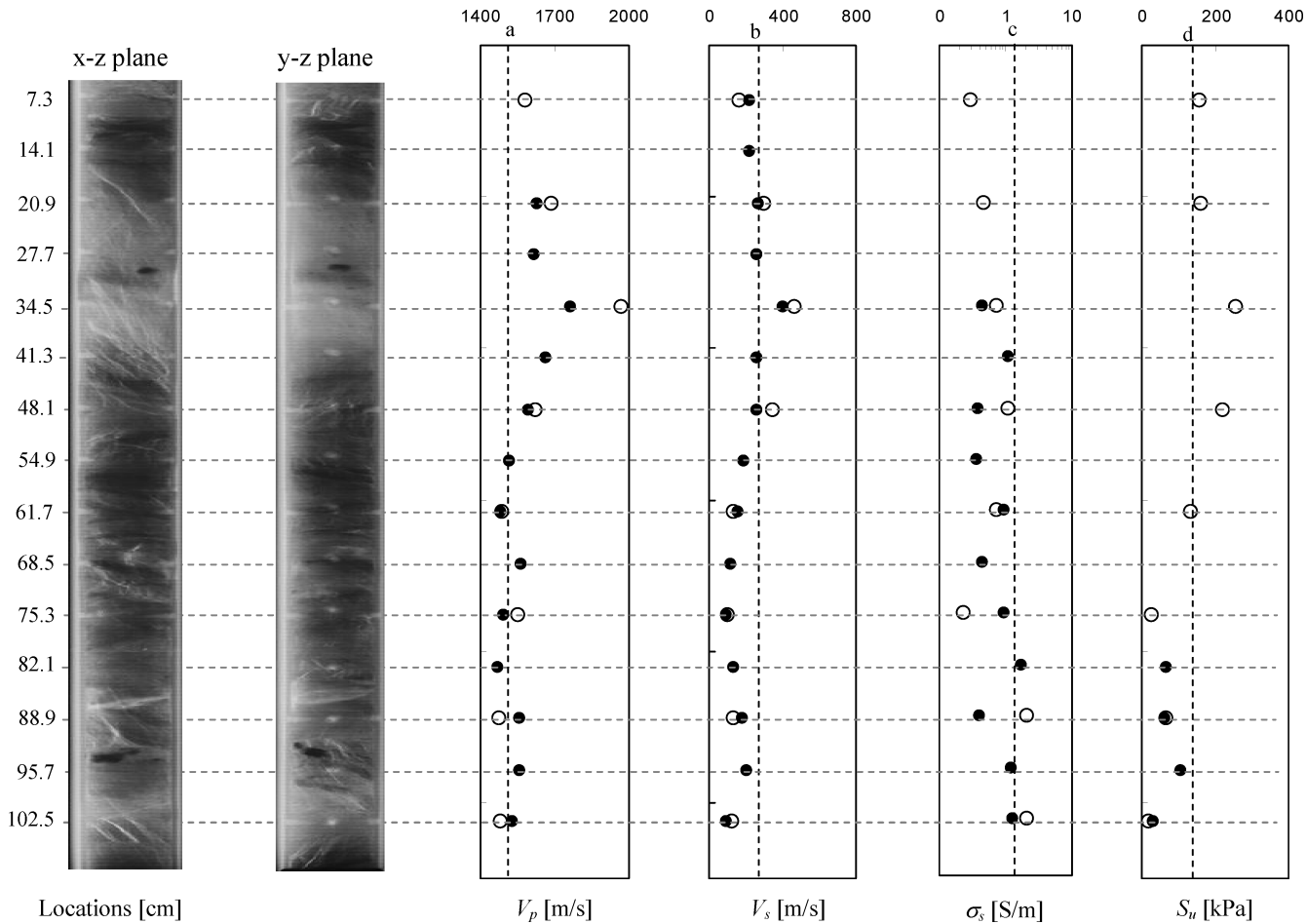


Figure 2. X-ray images and property profiles for specimen 21A-03E (HRC; X-ray images source: GeoTek, Inc.) along the x – z and y – z planes. Light colors indicate low-density materials, such as hydrates, while darker colors denote high-density sediments or inclusions. (●) Measured on the x – z plane. (○) Measured on the y – z plane. The electrical conductivity σ_s and the undrained shear strength S_u are the maximum values obtained in each penetration. Estimated reference values: (a) seawater P-wave velocity $V_p \sim 1500$ m/s, (b) S-wave velocity $V_s = 264$ m/s, (c) sediment conductivity $\sigma_s = 1.53$ S/m, and (d) undrained shear strength $S_u = 0.22\sigma' = 130$ kPa. Note that the highest S-wave velocity near 34.5 cm is captured directly through the hydrate lens. The dotted lines guide the measured location in X-ray images and corresponding material properties.

inclusions. The regularly spaced light-color rectangles along the core boundaries are the holes left after drilling and probe insertion in the IPTC. All specimens exhibit pronounced heterogeneity from milli- to centimeter scales. Horizontal layering features are perpendicular to the coring direction. Horizontal to near-vertical gas hydrate lenses are observed in all of the tested cores. Distinct vertical hydrate lenses bisect the upper part of the 21A-02Y core in Figure 4. High-density nodules are apparent in specimens 21A-03E (Figure 2) and 21A-02Y (Figure 4), and high-density layers are observed in specimen 21C-02E (Figure 3).

P-Wave Velocity. The constrained modulus is dominated by the bulk stiffness of water in saturated soft sediments.

Therefore, the P-wave velocity V_p in shallow sediments should be similar to the propagation velocity in seawater $V_p \sim 1500$ m/s, following Biot–Gassman asymptotic solution when the porosity is greater than ~ 0.4 . This is the selected reference value, and it is shown as a vertical dotted line in Figures 2–4. Velocities higher than this reference indicate high skeletal shear stiffness G associated with the presence of hydrates or cemented nodules. Especially high V_p values are found near the 34.5 cm location in Figure 2. These high V_p values coincide with the near-vertical hydrate lenses shown in the X-ray images.

S-Wave Velocity. The shear wave velocity $V_s = (G/\rho)^{1/2}$ reflects the soil skeletal shear stiffness G and the mass density ρ .

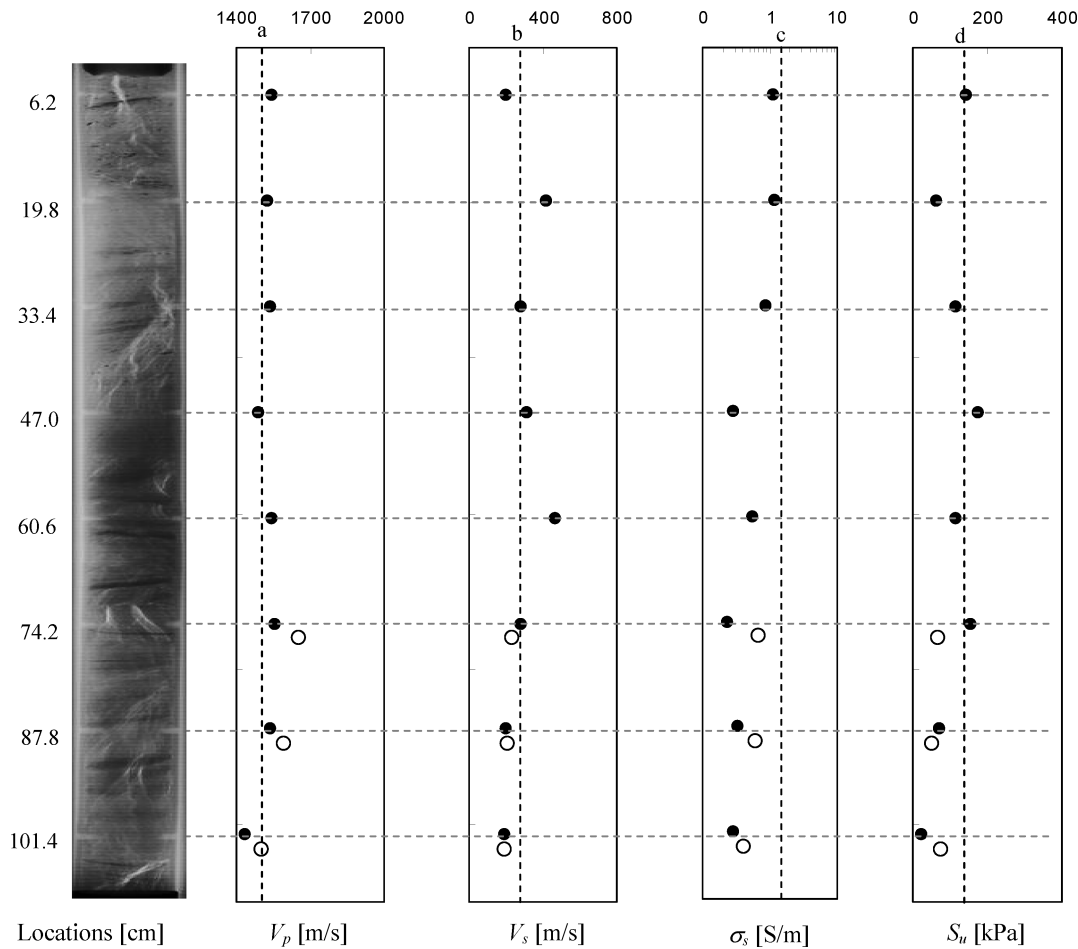


Figure 3. X-ray image and property profiles for specimen 21C-02E (HRC; X-ray image source: GeoTek, Inc.). The electrical conductivity σ_s and the undrained shear strength S_u are the maximum values obtained in each penetration. (○) Repeated measurements before degassing.

The mean effective stress $p'_o = (\sigma'_v + \sigma'_h)/2 = [(1 + K_o)/2]\sigma'_v$, where σ'_v and σ'_h are vertical and horizontal effective stress and $K_o = \sigma'_h/\sigma'_v$ is the lateral stress coefficient, on the polarization plane controls the skeletal shear stiffness in uncemented soils, as captured in semi-empirical models.¹³

$$V_s = \alpha \left(\frac{p'}{p_r} \right)^\beta \quad (1)$$

where the α factor is the shear wave velocity at $p' = 1$ kPa, the β exponent captures the sensitivity of the shear wave velocity to the state of stress, and $p_r = 1$ kPa is the reference pressure. The adopted reference value $V_s = 264$ m/s, shown as a dotted line in Figures 2–4, represents the velocity estimated for an uncemented, normally consolidated, high-plasticity sediment subjected to an estimated mean effective stress $p' = 457$ kPa (on the basis of the effective vertical stress $\sigma'_v = 590$ kPa and lateral earth pressure coefficient $K_o = 0.55$) using a factor $\alpha = 42$ m/s and exponent $\beta = 0.3$.¹⁴ This reference value is computed by assuming that sediments are at the *in situ* state of stress. While velocities below the reference value may be due to stress relaxation upon sampling, velocities above the reference are strong indicators of hydrates, stiffening the granular skeleton and overcompensating

for stress relaxation to the virtually zero effective stress condition of pressure cores. The measured shear wave velocity is higher than the reference value at several locations, particularly at 34.5 cm in Figure 2 and along the whole length of the core in Figure 4, suggesting the presence of hydrates.

Electrical Conductivity. The sediment electrical conductivity σ_s is determined by the pore fluid conductivity σ_f (ionic concentration and mobility), restricted by sediment porosity n , and enhanced by surface conduction in high specific surface clays in low σ_f systems. Archie's law can be fitted to most marine sediments $\sigma_s = A n^c \sigma_f$.¹⁵ The reference conductivity, $\sigma_s = 1.53$ S/m, shown as a dotted line in Figures 2–4, is estimated assuming a pore fluid conductivity $\sigma_f = 5$ S/m for seawater, porosity $n = 0.61$, and empirical parameters $A = 0.5$ and $c = 1.0$ (see similar estimates for Gulf of Mexico sediments¹¹). The estimated reference value is similar to conductivities measured in core 21C-02E after depressurization (Table 1). Most electrical conductivity values measured in the IPTC within the stability field of methane hydrates fall below the reference conductivity $\sigma_s = 1.53$ S/m, particularly in zones suspected of high hydrate volume fraction.

Undrained Shear Strength. The undrained shear strength S_u in uncemented normally consolidated sediments is a function of the *in situ* effective stress, the friction angle ϕ , and the sediment tendency to generate excess pore pressure

(13) Stokoe, K. H.; Lee, J. N.-K.; Lee, S. H.-H. *Characterization of Soil in Calibration Chambers with Seismic Waves*; Elsevier: Amsterdam, The Netherlands, 1992; p 363.

(14) Santamarina, J. C.; Klein, K. A.; Fam, M. A. *Soils and Waves*; John Wiley: New York, 2001; p 488.

(15) Archie, G. E. The electrical resistivity log as an aid in determining some reservoir characteristics. *Trans. AIME* **1942**, *146*, 54–62.

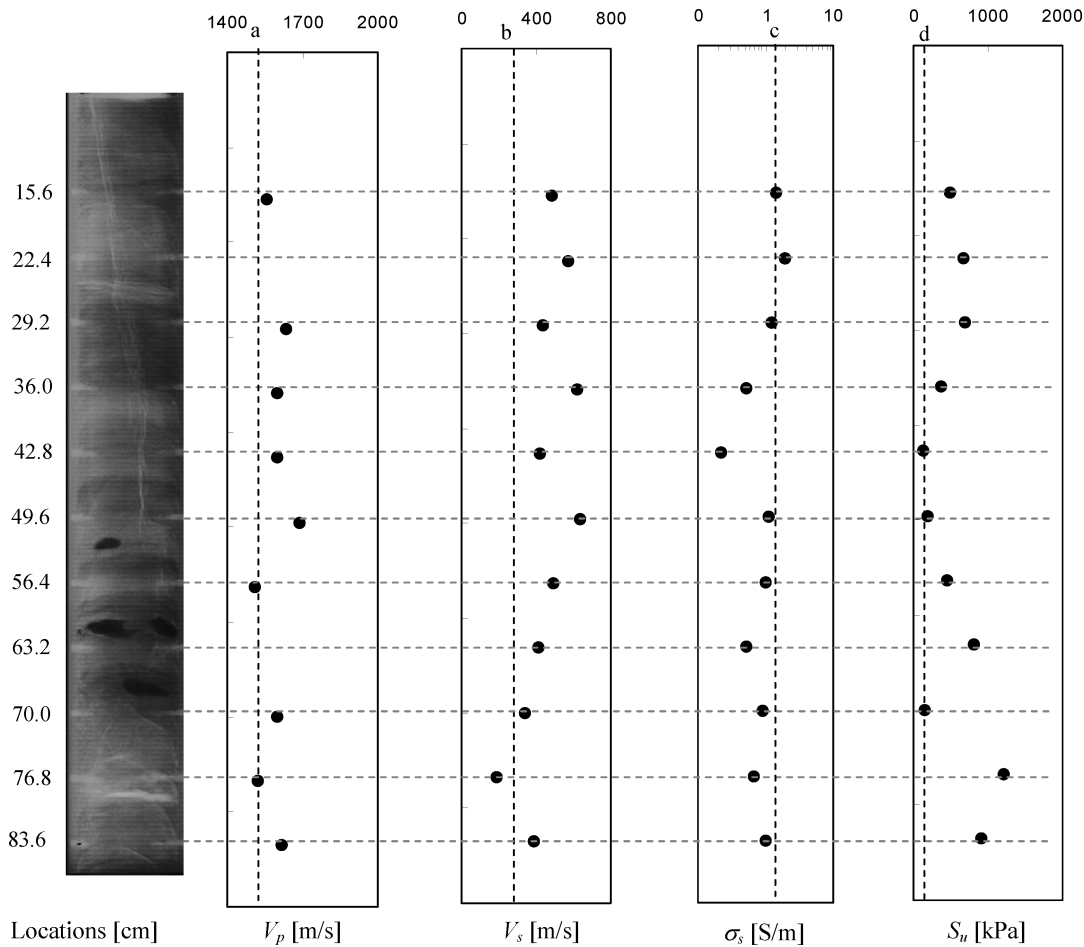


Figure 4. X-ray image and property profiles of specimen 21A-02Y (FPC; X-ray image source: GeoTek, Inc.). The dark nodules in the X-ray image are an indication of the presence of high-density nodules in the sediment. The electrical conductivity σ_s and the undrained shear strength S_u are the maximum values obtained in each penetration. Note that the scale of the undrained shear strength is different from the scale in Figures 2 and 3.

during shear. For uncemented normally consolidated clayey soils, the undrained shear strength can be estimated as $S_u = 0.22\sigma'_v$.¹⁶ The value $S_u \sim 130$ kPa for $\sigma'_v \cong 590$ kPa is adopted as the reference and shown as a dotted line in Figures 2–4. The undrained shear strength for cores 21A-03E and 21C-02E oscillates around the reference value (Figures 2 and 3). The undrained shear strength for core 21A-02Y in Figure 4 is much higher than the reference value. We also note that the measured undrained shear strength increases radially from the edge to the center of the core in all specimens. Note that sediments at the edge experience higher disturbance upon sampling and that stress is concentrated toward the center.

Controlled Depressurization of a Pressure Core. A 21C-02E core was sub-sampled with the length of 380 mm under pressure and used to simulate gas production by depressurization. Note that the IPTC chamber was filled with chilled water and that the entire system resided in the refrigerated container (~ 4 °C), which was supposed to be a nearly constant boundary temperature condition. P-Wave velocity V_p , electrical conductivity σ_s , sediment temperature T_s , and the volume of produced gas and water were continuously monitored at fixed locations, as shown in Figure 5. The controlled depressurization test started with a gradual reduction of the hydrostatic fluid pressure at an average rate of 0.18

MPa/min, until P – T conditions reached the hydrate phase transformation boundary ($P = 3.85$ MPa and $T = 39$ °C for pure water conditions). The pressure was dropped in steps for each reduction. Once hydrate dissociation started, the rate of depressurization was reduced to about 0.025 MPa/min (Figure 6a), indicated by line A. The produced gas was collected using the inverted graduated cylinder. The inverted cylinder was fully submerged within an outer container and connected to the IPTC through saturated tubing. During the depressurizing test, the gas released by the hydrate dissociation replaced the water in the inverted cylinder to read the gas volume. Any water released during hydrate dissociation increased the level in the outer container to read the volume of water from the IPTC system.

X-ray Images (Figure 5). The image gathered before depressurization clearly shows near-vertical hydrate lenses and horizontal stratification. Lenses are not observed within images obtained after depressurization, and the stratification becomes fuzzier probably as a result of gas expansion and fluid/gas migration. Note that both images were taken at the same orientation for direct comparison. The sediment expansion is about 1 cm toward the lower open end, and an extensive network of discontinuities is observed. It is supposed that the hydrate dissociation, expansion of liberated gas, and subsequent migration driven by depressurization may cause the discontinuity.

(16) Mesri, G. Re-evaluation of $S_u = 0.22\sigma'_v$ using laboratory shear tests. *Can. Geotech. J.* **1989**, *26* (1), 162–164.

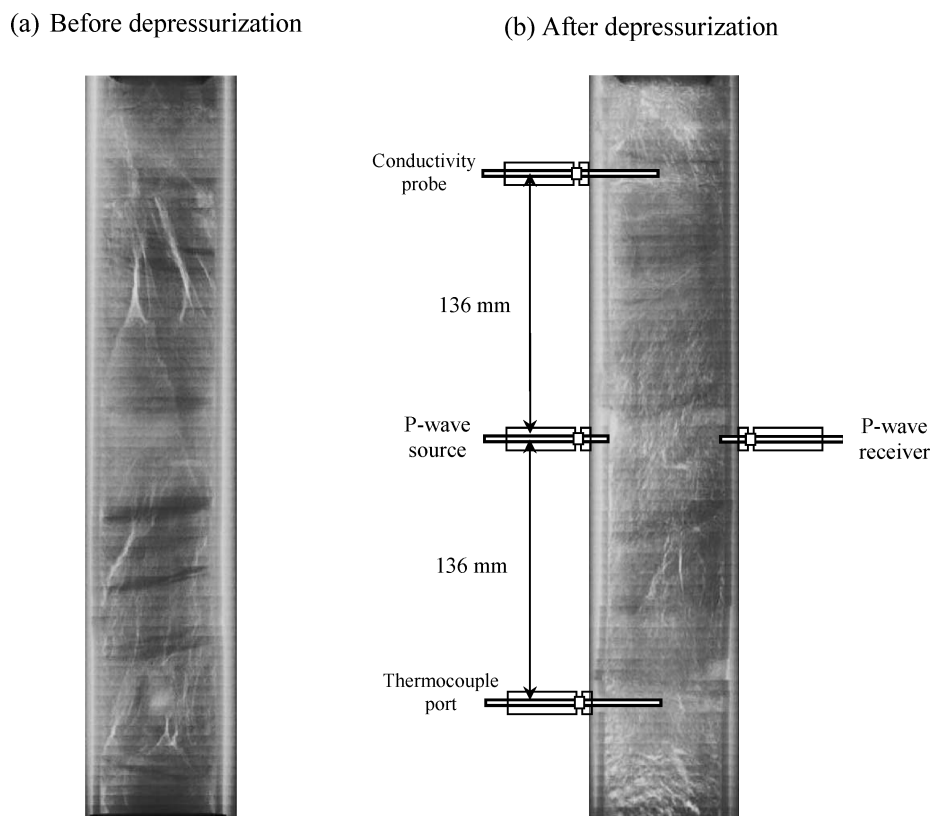


Figure 5. Instrumentation for the degassing test. Specimen sub-sampled under pressure from core 21C-02E. (a) X-ray image before depressurizing. The white color indicates the presence of hydrates in the specimen core. (b) X-ray image after depressurizing and position of the instrumented probes.

Temperature (Figure 6b). The sediment temperature T_s remains almost constant during the early stage of depressurization, indicating the absence of the gas phase inside the core. Once hydrates begin dissociating, the endothermic event absorbs heat from the surroundings and the measured temperature drops below 0 °C. The temperature drop is accentuated by further depressurization in the presence of liberated gas, denoted by line B. The exothermic peaks near $T = 0$ °C may be attributed to ice formation and temperature rebound toward the equilibrium condition.

P-Wave Data (Figures 6c and 7). The amplitude of P-wave signals vanishes soon after P – T conditions reach the phase boundary. The first arrival of P-wave indicates $V_p \sim 1510$ m/s (Figure 7) and remains constant until the hydrates were dissociated. As gas was liberated (between point A and B, corresponding lines A and B in Figure 6), the fluid bulk stiffness decreases and the acoustic attenuation prevailed, resulting in the decay of the P-wave amplitude (Figure 7). Note that that IPTC data for other pressure core characterization shows a gradual decrease of shear wave velocity during hydrate dissociation.¹⁷

Electrical Conductivity (Figure 6d). The electrical conductivity decreases during early stages of dissociation, followed by a decisive increase toward the end of the test. The electrical conductivity signature reflects the complex interaction among multiple coexisting processes: liberation of ion-free water during hydrate dissociation, temperature-dependent ionic mobility,

ice formation and ion exclusion, and development of a free gas phase.

Produced Gas (Figure 6e). A total of 23.5 L of gas was collected at atmospheric pressure. The volume of methane gas V_g at atmospheric pressure and 4 °C is related to the volume of hydrate V_h as $V_g = 173V_h$ (this relationship is estimated at 4 °C under 1 atm¹⁸). The produced gas, therefore, corresponds to a hydrate volume $V_h = 136$ cm³. Note that it is assumed that the volume of collected gas comes from the hydrate only. Any dissolved gas phase that may be liberated by depressurization is not counted, so that this estimation delineates upper bounds in the volumetric fraction of the hydrate $VF_h (= V_h/V_{\text{specimen}})$. The estimated value of VF_h is 18.2% (380 mm in length and 50 mm in diameter, so that $V_{\text{specimen}} = 746$ cm³).

Nonconcurrent Changes (Figure 6). Early signs of dissociation were captured at different times by the different sensors; electrical conductivity reacts first ($t = 64$ min – line A), followed by P-wave amplitude and sediment temperature ($t = 82$ min – line B). These time lags may be caused by the different sensor locations along the specimen length, heterogeneous hydrate volume fractions, and distinction between local measurements (temperature and electrical conductivity, near the core center) versus path-averaging P-wave measurements. In addition, the specimen is not in equilibrium during fast depressurization, and the dissociation front advances across the specimen, reaching the various sensors at different times.

Evolution of Dissociation in the P – T Space (Figure 8). The evolution of pressure is plotted against the temperature in

(17) Yun, T. S.; Lee, C.; Lee, J. S.; Bahk, J.-J.; Santamarina, J. C. A pressure core based characterization of hydrate-bearing sediments in the Ullung Basin, East Sea. *J. Geophys. Res., [Solid Earth]* **2010**, manuscript under review.

(18) Kwon, T.-H.; Cho, G.-C.; Santamarina, J. C. Gas hydrate dissociation in sediments: Pressure–temperature evolution. *Geochem., Geophys., Geosyst.* **2008**, 9, No. Q03019.

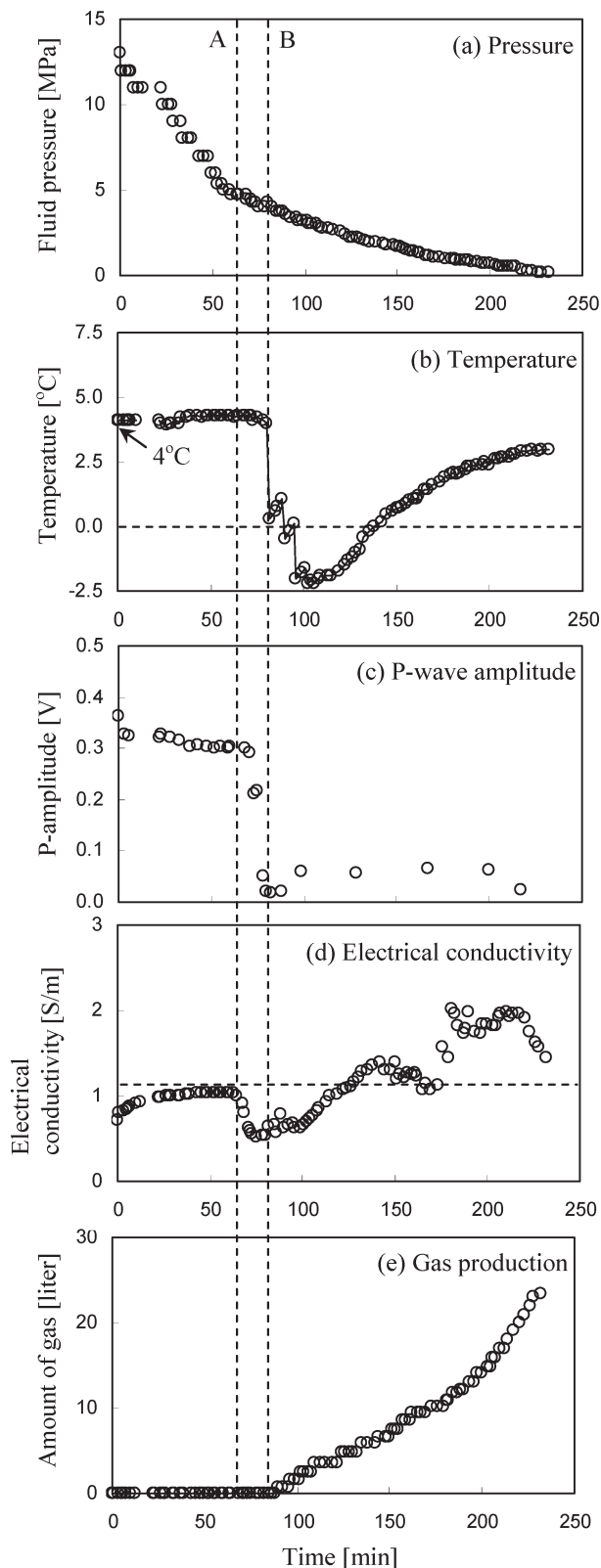


Figure 6. Evolution of properties and volume of gas (at atmospheric pressure) collected during controlled depressurization. Line A indicates the change of the depressurization rate, and line B denotes when the temperature changes and the gas production starts.

Figure 8. The stability curve for methane hydrates is constructed for the case of pure water and ionic concentration of 3 wt % using CSMHYD software.

While gas hydrate dissociation in slow tests remains on the phase transformation boundary until complete dissociation, the implications of separate sensor location and the advancing dissociation front discussed above result in a more complex P – T response in this relatively fast test.

Discussion

The characterization of hydrate-bearing sediments faces multiple difficulties, even when pressure cores are obtained. Issues related to the validity and limitations of the gathered data are explored in this section, including measurement repeatability, the inherent temporal and spatial scales in the cores and in the IPTC measurements, verification with physical bounds, and the consequences associated with effective stress change.

Sediment Characterization. Index properties provide crucial particle–fluid information and allow us to estimate engineering design parameters using the accumulated knowledge in the geotechnical engineering field. Values listed in Table 1 are used to estimate the following geomechanical properties for these sediments without hydrates: (1) The liquid and plastic limits correspond to illite minerals; this is in agreement with the specific surface and previous knowledge of these sediments. (2) The empirical correlation based on the plastic limit, plastic index, and porosity evaluates the hydraulic conductivity of clayey soils.¹⁹ The estimated value is $k \sim 5 \times 10^{-8}$ cm/s. (3) The water content ($w_c = 65\%$), liquid limit ($w_L = 75\%$), and plastic limit ($w_P = 35\%$) allow us to estimate the following deformation and strength parameters: compression index C_c , 0.46–0.6;^{20–23} friction angle ϕ , 28° ;²³ residual friction angle ϕ_r , 10 – 16° ;²⁴ and normalized undrained shear strength S_u/σ'_v , 0.22.¹⁶

The hydraulic and geomechanical properties estimated above should be gathered from the undisturbed samples, which are hardly obtainable in practice, particularly for the hydrate-bearing sediments. However, index properties are independent of the effect of sample disturbance (a detailed discussion on sampling effects is presented later). Therefore, these first-order estimates of engineering properties based on the index properties provide valuable insight for the samples before advanced laboratory and *in situ* measurements become available. Furthermore, the compression index, friction angle, shear strength, and hydraulic conductivity values are inevitable input for the numerical study and design parameters for borehole stability and production technology of hydrate-bearing sediments.

Repeatability. Two cores were reinserted into the chamber and tested for duplicate characterization. The full core 21A-03E was rotated 90° to repeat measurements at a second plane (e.g., x – z and y – z planes). The sub-sampled 21C-02E was reinserted without rotation and slightly offset along the same measurement plane. Data superimposed on Figures 2 and 3 (e.g., ● and ○) show relatively good agreement. Note

(19) Carrier, W. D.; Beckman, J. F. Correlation between index tests and the properties of remolded clays. *Geotechnique* **1984**, *34* (2), 211–228.

(20) Carrier, W. D. Consolidation parameters derived from index tests. *Geotechnique* **1985**, *35* (2), 211–213.

(21) Mesri, G.; Stark, T. D.; Ajlouni, M. A.; Chen, C. S. Secondary compression of peat with or without surcharging. *J. Geotech. Geoenviron. Eng.* **1997**, *123* (5), 411–420.

(22) Terzaghi, K.; Peck, R. B. *Soil Mechanics in Engineering Practice*, 2nd ed.; John Wiley and Sons, Inc.: New York, 1967; p 729.

(23) Terzaghi, K.; Peck, R. B.; Mesri, G. *Soil Mechanics in Engineering Practice*, 3rd ed.; John Wiley and Sons, Inc.: New York, 1996; p 549.

(24) Stark, T. D.; Eid, H. T. Drained residual strength of cohesive soils. *J. Geotech. Eng.* **1994**, *120* (5), 856–871.

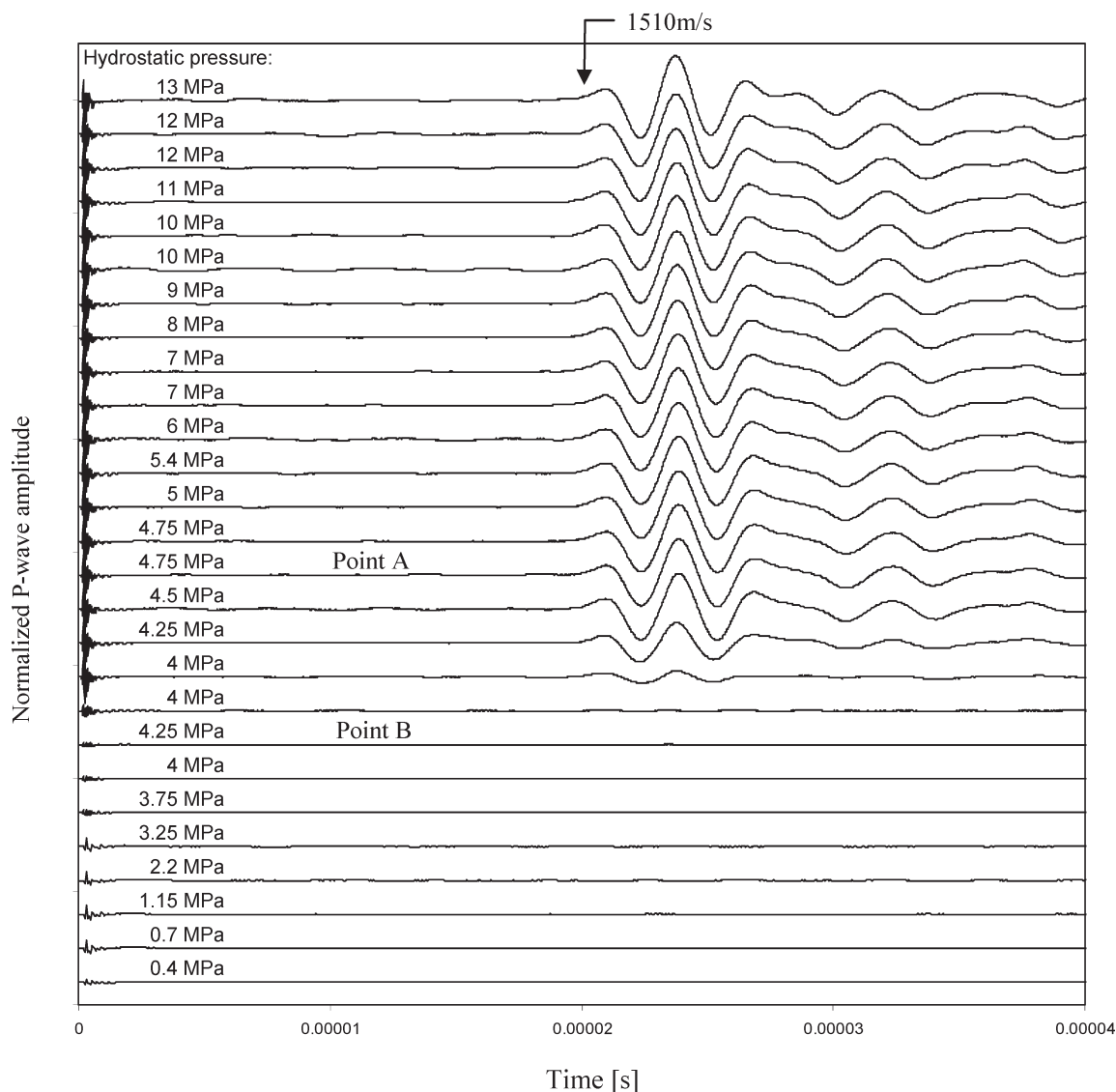


Figure 7. Evolution of P-wave traces during gas hydrate dissociation. The P-wave measurement sensor is located at the center of the specimen. The chamber temperature is kept at 4 °C.

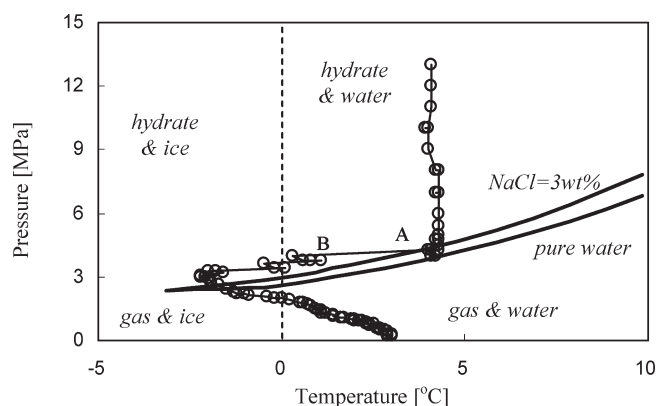


Figure 8. Gas production test by controlled depressurization. Pressure and temperature evolution. The P – T trend does not remain on the phase boundary during dissociation because of separate locations between sensors.

that the tested specimen did not experience dissociation when repeated measurements were conducted. Beyond

experimental difficulties, discrepancies in the data (e.g., wave velocity measured at 34.5 cm in Figure 2) may reflect the non-homogeneous spatial distribution of hydrate and high-density nodules and the preferential orientation of hydrate lenses.

Scales and Upscaling. The following length and time scales relate to measurements conducted in the IPTC. (1) P-waves: mean frequency, 1 MHz; corresponding wavelength, ~ 1.5 mm. (2) S-waves: mean frequency, 100 kHz; corresponding wavelength, ~ 3 mm. (3) The electrical needle probe length scale is the needle diameter of 2.5 mm. (4) The shear strength cone length scale is about 3 times the cone diameter or 18 mm.

It is concluded that the measured properties correspond to sub-centimeter length scales. Therefore, careful consideration must be given to upscaling the IPTC data before comparing it against field measurements and for applications that often exceed the meter length scale.

Upper and Lower Bounds: Verification. The bulk stiffness K of the sediment is a function of the constrained modulus M and the shear modulus G and can be expressed in terms of the

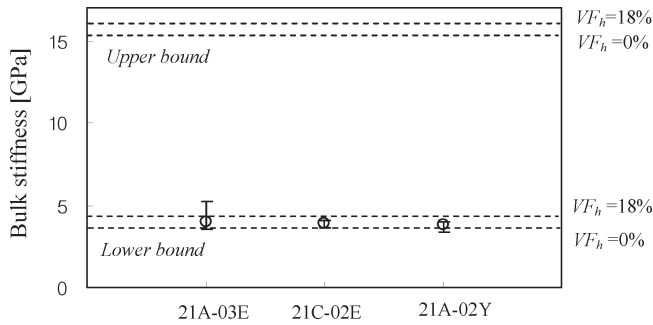


Figure 9. Verification of elastic wave velocity data in terms of bulk stiffness (before depressurization). Upper and lower bounds for $VF_h = 0$ and 18% computed using parallel and series models.

measured V_p and V_s

$$K = M - \frac{4}{3}G = V_p^2 \rho - \frac{4}{3}V_s^2 \rho \quad (2)$$

where ρ is the sediment mass density. Upper and lower bounds for the bulk stiffness can be computed from the sediment components and their volume fractions, assuming parallel and series configurations, respectively. These bounds are wider than the Hashin–Strikman bounds

$$K_s^{LB} = \left[\frac{1-n}{K_m} + \frac{n-VF_h}{K_w} + \frac{VF_h}{K_h} \right]^{-1} \quad \text{lower bound, series} \quad (3)$$

$$K_s^{UB} = (1-n)K_m + (n-VF_h)K_w + VF_h K_h \quad \text{upper bound, parallel} \quad (4)$$

where subscripts h, m, w, and s correspond to hydrate, mineral, water, and sediment, respectively. Figure 9 shows the computed bulk stiffness using measured wave velocities (●) and the bounds for hydrate volume fraction $VF_h = 0$ and 18% (K_m , 36 GPa; K_f , 2.3 GPa; and K_{hyd} , 5.6 GPa²⁵). Results show that measured velocities do not violate the physical bounds, the hydrate volume fraction is generally lower than $VF_h = 18\%$, and the internal sediment structure resembles a series-type rather than parallel-type configuration. A similar observation is reported by Lee²⁶ for a wide range of hydrate-bearing sediments when the hydrate volume fraction is less than $VF_h \leq 30\%$. The estimated bulk stiffness often indicates beyond the lower bound of $VF_h = 18\%$ because of the highly heterogeneous nature of hydrate structures (e.g., 21A-03E in Figure 9).

The lower bound for electrical conductivity approaches zero because the mixture conductivity in the series configuration is restricted by the near-zero mineral and gas hydrate conductivities. The upper bound corresponds to the parallel configuration in the absence of surface conduction and reduces to $\sigma_s^{UB} \approx (n - VF_h)\sigma_n$. Upper bound estimations are $\sigma_s = 3.1$ S/m for $VF_h = 0\%$ and $\sigma_s = 2.15$ S/m for $VF_h = 18\%$. Measured values range from 0.04 to 2.09 S/m. This analysis delineates the acceptable range of values in electrical conductivity for hydrate-bearing sediments during the laboratory investigation and *in situ* evaluation.

(25) Yun, T. S.; Francisca, F. M.; Santamarina, J. C.; Ruppel, C. Compressional and shear wave velocities in uncemented sediment containing gas hydrate. *Geophys. Res. Lett.* **2005**, *32*, No. L10609.

(26) Lee, J.-Y. Hydrate bearing sediments: Formation and geophysical properties. Ph.D. Thesis, Georgia Institute of Technology, Atlanta, GA, 2007.

Effective Stress. Measurements in the IPTC were performed at a hydrostatic pressure that maintains the specimen within the hydrate stability field by connecting the entire system to the pressure-controlled water pump. However, the specimen is subjected to a very low and uncertain effective stress; the linear locks in some longitudinal stress (through friction) and radial stress (related to the longitudinal stress by the Coulomb strength criterion), but their magnitudes are strongly dependent upon minor yet decisive operational details and cutter design. This situation calls for a careful analysis of the meaning of effective stress-dependent properties, such as V_s and S_u when measured in the IPTC. In this section, we show that measurements reflect *in situ* values when sediments preserve volume, as a first condition; the relevance of structure preservation is discussed in the following section.

From Stress- to Volume-Dependent Properties. Stress-dependent properties can be expressed in terms of porosity n or void ratio $e = n/(1-n)$. Once we express the *in situ* void ratio e_o as a function of the mean effective stress $p'_o = (\sigma'_h + \sigma'_v)/2$, the soil is subjected to

$$e_o = e_{p_r}^{NC} - \lambda \ln \left(\frac{p'_o}{p_r} \right) \quad \text{unloading response} \quad (5)$$

where $p_r = 1$ kPa is a reference pressure, $e_{p_r}^{NC}$ is the void ratio at the reference pressure, and λ is the sediment compressibility. Then, expressions that relate strength and stiffness to *in situ* effective stress p'_o are rewritten in terms of e_o .

Let us consider the undrained strength S_u . It must satisfy the Coulomb failure criterion, and the void ratio at critical state failure e_{cs} (e.g., failure state of the specimen undergoes shear deformation without changes in volume, effective stress, and shear strength) must be the same as the initial void ratio $e_{cs} = e_o$ because shear is imposed under undrained conditions

$$S_u = p'_f \sin \phi \quad \text{Coulomb failure criterion} \quad (6)$$

$$e_{cs} = e_{p_r}^{cs} - \lambda \ln \left(\frac{p'_f}{p_r} \right) = e_o \quad \text{critical state shear failure} \quad (7)$$

where $e_{p_r}^{cs}$ is the critical state void ratio at the reference pressure p_r . Extracting the mean effective stress at failure p'_f from eq 6 and replacing in eq 7 gives the following expression for the undrained shear strength S_u as a function of the *in situ* void ratio e_o .

$$S_u = \exp \left(\frac{e_{p_r}^{cs} - e_o}{\lambda} \right) \sin \phi p_r \quad (8)$$

Similarly, a void-ratio-dependent relationship for small-strain shear wave velocity can be obtained by extracting the *in situ* mean stress p'_o from eq 5 and replacing it in eq 1.

$$V_s = \alpha \left[\exp \left(\frac{e_{p_r}^{NC} - e_o}{\lambda} \right) \right]^\beta \quad (9)$$

The validity of void-ratio-dependent stiffness is documented by Klein and Santamarina.²⁷

Volume Preservation upon Sampling. The compressibility of clayey sediments during loading is 5–10 times greater than

(27) Klein, K.; Santamarina, J. C. Soft sediments: Wave-based characterization. *Int. J. Geomech.* **2005**, *5* (2), 147–157.

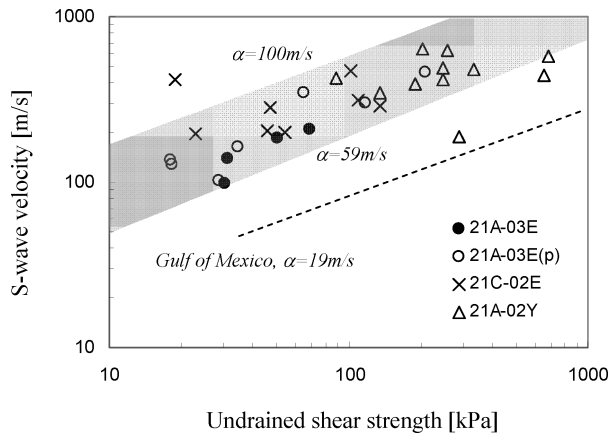


Figure 10. S-Wave velocity versus undrained shear strength (15 mm deep penetration). The trend shown for Gulf of Mexico sediments recovered 0–300 mbsf and water depth ~1400 m.¹¹

their expansivity during unloading.²³ Therefore, the void ratio $e = n/(1 - n)$ of recovered clayey sediments reflects the maximum effective stress felt by the sediment. Then, eqs 8 and 9 indicate that undrained shear strength and shear wave velocity values measured in the IPTC provide field-relevant information for clayey sediments, including the sediment reported in this paper. It has been suggested that the production of methane gas from hydrates in sandy sediments seems to be more feasible in terms of economic feasibility and sediment stability. Yet, the case of sandy sediments is more complex because they have low compressibility λ and the void ratio keeps almost no memory of past effective stress. Furthermore, these sediments are most susceptible to experience volume and fabric changes during sampling. On the other hand, available experimental results²⁶ show that sandy sediments will preserve stiffness upon unloading when the hydrate volume fraction is high ($VF_h \geq 3\%$) and should be adequate for characterization within the IPTC.

When the hydrate-bearing sediments were recovered by the pressure coring technique, the volume change was unavoidable (e.g., expansion because of the *in situ* stress release). Thus, the measured properties after inherent sample disturbance did not fully reflect the *in situ* geomechanical and physical properties. This discrepancy can be further investigated using eqs 5–9 to infer the *in situ* properties with supplementary evaluation of on-board measurements.

Correlation between Small- and Large-Strain Values. The void ratio-dependent functions for V_s and S_u (eqs 8 and 9) suggest a positive correlation between the small-strain V_s and the large-strain S_u , through the common causal link to effective stress. This is corroborated in Figure 10, where all V_s and S_u data gathered from the three cores before depressurization are shown (the symbols within the gray region). The reported values of α (100 and 59 m/s) delineate the upper and lower bounds for the NGHP sediments. For comparison, the trend for data gathered with Gulf of Mexico sediments¹¹ is superimposed on the figure (dotted line). Differences among these trends reflect differences between the two sediments as readily seen in index properties (specific surface, friction angle, and liquid and plastic limits). More importantly, hydrates were present in the Indian pressure cores but not in the Gulf of Mexico cores. Additionally, the empirical correlation between V_p and V_s is made to guide the relevance in the pressure cores characterized in this study (Figure 11). Two lines approximately delineate the upper and

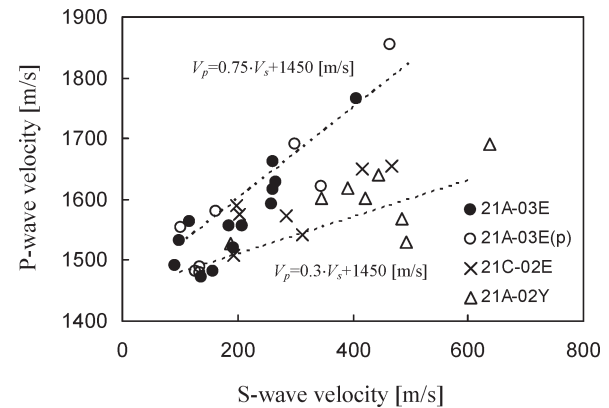


Figure 11. Correlation between P- and S-wave velocities. The upper and lower bounds delineate the tolerable range of wave velocities measured for the tested site.

lower bounds. The gradient ranges between 0.3 and 0.75, guiding the acceptable values of wave velocities for the tested sites.

Sampling Effects. While the previous analysis assumes that sampled fine-grained sediments preserve the *in situ* porosity, the imposed strain level during sampling may erase the effects of aging and cementation. Even block-sampling methods cause unavoidable stress release from the *in situ* K_0 state to an isotropic state that may range from 50 to 90% of the initial mean effective stress for saturated soft clayey sediments.^{28–31} Still, available evidence suggests that the impact of sampling on sediment properties is less pronounced in soft plastic sediments than in stiffer and coarser sediments.^{32–35}

The probability of capturing the sub-vertical and vertical hydrate veins observed in the X-ray images appears to be very low during pressure core sampling. Thus, observed topological features of hydrates upon sampling may not fully reflect the *in situ* condition. This observation also suggests the following causally related sequence of events during pressure core recovery: effective stress loss → skeletal expansion hindered by sediment suction → decrease in the fluid pressure inside the specimen → hydrate dissociation → gas-driven sediment fracture → hydrate lens formation when conditions return to the stability field of hydrates. Note that energy transfer required to make sequential events happen needs further investigation for pressure core sampling on hydrate-bearing sediments.

(28) Hight, D. W.; Boese, R.; Butcher, A. P.; Clayton, C. R. I.; Smith, P. R. Disturbance of the Bothkennar clay prior to laboratory testing. *Geotechnique* **1992**, 42 (2), 199–217.

(29) Ladd, C. C.; Lambe, T. W. The strength of undisturbed clay determined from undrained test. *ASTM Spec. Tech. Publ.* **1963**, 361, 342–371.

(30) Santagata, M. C.; Germaine, J. T. Sampling disturbance effects in normally consolidated clays. *J. Geotech. Geoenviron. Eng.* **2002**, 128 (12), 997–1006.

(31) Skempton, A. W.; Sowa, V. A. The behavior of saturated clays during sampling and testing. *Geotechnique* **1963**, 13 (4), 269–290.

(32) Kimura, T.; Saitoh, K. Effect of sampling disturbance on undrained strength of cohesive soils. *Geotech. Eng.* **1984**, 15 (1), 37–57.

(33) Matsuo, M.; Shogaki, T. Effects of plasticity and sample disturbance on statistical properties of undrained shear strength. *Soils Found.* **1988**, 28 (2), 14–24.

(34) Siddique, A.; Farooq, S. M.; Clayton, C. R. I. Disturbances due to tube sampling in coastal soils. *J. Geotech. Geoenviron. Eng.* **2000**, 126 (6), 568–575.

(35) Hvorslev, M. J. *Subsurface Exploration and Sampling of Soils for Civil Engineering Purpose*; American Society of Civil Engineers (ASCE) Waterways Experiment Station: Vicksburg, MS, 1949; p 465.

Implications of IPTC Results. The IPTC is an unprecedented tool for the quantification of physical properties of gas hydrate-bearing sediments recovered by pressure coring. Within the limitations outlined above, IPTC results combine with borehole logging data, with physical properties obtained using synthetic samples (which do not necessarily capture the formation history *in situ* or use alternative hydrate formers) and parameters gathered using remolded specimens (including index properties, specimens recovered by conventional coring or after depressurization of pressure cores), to provide a comprehensive understanding of hydrate-bearing sediments *in situ*. Properties measured in such studies, including IPTC, correspond to the centimeter scale and must be up-scaled to develop adequate material models for stability analyses and reservoir simulations.

A salient advantage of the IPTC is the ability of monitoring the evolution of the sediment and physical properties during depressurization and degassing, allowing for unique insight of the dynamic interplay among multiple phases and concurrent processes.

Sediment Disturbance during Degassing. Hydrate dissociation into gas and liquid pore fluid is accompanied by pronounced volume expansion. In coarse sediments, the excess pore fluid pressure generation could be low in the absence of clogged porosity (i.e., free draining) and suction is also low; therefore, degassing does not necessarily alter the sediment fabric. This is not the case in fine-grained sediments. The gas-liberated dissociation generates capillary forces that alter the sediment structure, forming microfractures (as observed in Figure 5), and provided the path for gas migration. However, the pre-existing hydrate lenses as discontinuity provide preferential paths and have a possibility to be extended to further facilitate gas migration.^{36,37}

Freshening or the decrease in the ionic concentration with the increased availability of water also alters interparticle electrical forces in clayey sediments. While this effect is minor relative to massive fracturing because of gas expansion, a lower ionic concentration does affect double-layer phenomena, index properties (e.g., Atterberg limits), and the contribution of surface conduction to electrical conductivity.

Therefore, the interplay between gas-expansion-driven sediment disturbance and the creation of a preferential gas migration path plays a significant role in sample disturbance that eventually affects the physical and mechanical properties of sediments measured during the degassing process (Figures 6 and 7).

Conclusions

This paper documents the most comprehensive geophysical characterization of pressure cores attempted to date, whereby P-wave velocity V_P , S-wave velocity V_S , electrical conductivity σ_s and undrained strength S_u were measured on three hydrate-bearing pressure cores. The IPTC provides the unprecedented opportunity to measure properties while keeping specimens in the stability field throughout the recovery and measurement process.

The sediments in Krishna–Godavari Basin consist of high plasticity clays with specific surface $S_a \sim 90 \text{ m}^2/\text{g}$.

(36) Mahadevan, J.; Sharma, M. M.; Yortsos, Y. C. Capillary wicking in gas wells. *SPE J.* **2007**, *12* (4), 429–437.

(37) Seol, Y.; Kneafsey, T. J. X-ray computed-tomography observations of water flow through anisotropic methane hydrate-bearing sand. *J. Pet. Sci. Eng.* **2009**, *66* (3–4), 121–132.

Horizontal and sub-vertical hydrate lenses cut through the specimens. The hydrate volume fraction in the pore space is about $VF_h = 28\%$ for the tested pressure cores in this study (site NGHP-01-21).

Reference values for measured properties were estimated for the normally consolidated and uncemented sediment without hydrates using index properties and known correlations. The presence of hydrates is recognized when measured P-wave velocity, S-wave velocity, and undrained strength values fall below reference values, while the electrical conductivity remains below proposed reference values. The measured properties fluctuate along the length of the core, indicating a pronounced variability in hydrate distribution.

The IPTC allowed for the first production-monitoring exercise ever attempted with natural hydrate-bearing sediments. The evolution of physical properties agrees with trends expected for depressurization–dissociation but also hints at complex interactions among coexisting processes. Data interpretation must take into consideration the physical nature of the measurement and the spatial position of instruments with respect to the dissociation front.

Several caveats are identified: (1) The measured properties correspond to local, sub-centimeter length scale characteristics, and proper upscaling is required for field applications. (2) While pore fluid pressure is maintained within the stability field of hydrates, the effective stress is almost zero in the specimen. (3) Sampling the pressure core inevitably causes stress relaxation and ensuing strains and may result in the instability of hydrates. (4) In clayey soils, porosity tends to preserve the memory of the maximum effective stress experienced by the sediment and measured small- and large-strain properties can be related to field conditions based on the supplementary experimentation and analysis; this will not be the case in uncemented sands with low hydrate volume fraction, because they will lose most memory of *in situ* conditions and formation history.

Acknowledgment. Support for this research was provided by a contract to J.C.S. from the Joint Industry Project for Methane Hydrate, administered by E. Jones at Chevron, with funding from award DE-FC26-01NT41330 from the National Energy Technology Laboratory of the Department of Energy, and additional funds from the Goizueta Foundation. Jaewon Jang at Georgia Tech gathered the engineering index property of the sediments. Peter Schultheiss, Melanie Holland, and Matt Druce at GeoTek, Inc. provided technical support during field testing in Singapore. All findings are those of the authors and do not reflect the views of funding agencies or technical support personnel.

Nomenclature

- ρ = mass density (kg/m^3)
- ϕ = friction angle (deg)
- β = model factor
- α = model factor (m/s)
- κ^* = complex dielectric permittivity
- σ_{Π} = electrical conductivity of pore fluid (S/m)
- σ'_h = horizontal effective stress (Pa)
- σ'_s = electrical conductivity of sediment (S/m)
- σ'_v = vertical effective stress (Pa)
- A = parameter in Archie's law
- c = parameter in Archie's law
- C_c = compression index
- e_o = *in situ* void ratio
- $e_{p_r}^{\text{NC}}$ = void ratio at the reference pressure

e_{cs} = void ratio at critical state failure
 G = shear stiffness (Pa)
 I_p = plastic index
 K = bulk stiffness (Pa)
 K_o = lateral earth pressure coefficient (σ'_h/σ'_v)
 M = constrained modulus (Pa)
 n = porosity
 P = pressure (Pa)
 p' = mean effective stress (Pa)
 p_r = reference pressure (1 kPa)

S_a = specific surface
 S_u = undrained shear strength (Pa)
 T = temperature (°C)
 V = volume (m³)
 VF_h = volumetric fraction of hydrates (%)
 V_p = P-wave velocity (m/s)
 V_s = S-wave velocity (m/s)
 w_c = gravimetric water content (%)
 w_L = liquid limit (%)
 w_P = plastic limit (%)